This is the Pre-Published Version.

Y. He, M. Wang and Z. Xu, "Coordinative Low-Voltage-Ride-Through Control for the Wind-Photovoltaic Hybrid Generation System," in IEEE Journal of Emerging and Selected Topics in Power Electronics, vol. 8, no. 2, pp. 1503-1514, June 2020, DOI:10.1109/JESTPE.2019.2958213.

Coordinative Low-Voltage-Ride-Through Control for the Wind-Photovoltaic Hybrid Generation System

Yufei He, *Student Member, IEEE*, Minghao Wang, *Member, IEEE*, Zhao Xu, *Senior Member, IEEE*

***Abstract*—The wind-photovoltaic (PV) hybrid renewable energy system (HRES), which consists of permanent magnet synchronous generators (PMSG) and PV arrays, is becoming a cost-effective electric source for powering islanded areas. However, high penetration of renewables makes the power system vulnerable to transient voltage faults, which undermines the stability of the future inverter-dominated grid. To address this issue, a coordinative low-voltage-ride-through (LVRT) control scheme is proposed for the operation of the wind-PV HRES in this paper. This control scheme will exploit the maximum energy inertia of the HRES for incorporating the power imbalance between the faulted grid and the renewable generators. An optimization problem is formulated to maximize the renewable energy harvesting within the operational and environmental limitations. To cope with different working conditions, four control processes are coordinated in an optimized manner during the LVRT period, namely (i) Adaptive DC-link voltage control, (ii) PMSG rotating speed control, (iii) PV energy curtailment control, and (iv) Blade pitch angle control. Besides, this control scheme applies a direct output control that can generate stable and accurate current as per grid code requirements. The results of the hardware-in-the-loop (HIL) experiment and the MATLAB-Simulink simulation are provided to verify the effectiveness of the proposed control scheme.**

***Index Terms*— Hybrid renewable energy system, low-voltage-ride-through, power system faults, smart grid.**

I. Introduction

THE depletion of fossil energy forces the power industries to integrate the renewable energy sources to the power systems. Typically, PMSG-based wind energy conversion systems (WECS) and PV generation systems are prevailing in the modern power grids. They deliver volatile and intermittent energy to the grid, which threatens the grid stability and limits their scale of integration [1], [2]. In order to pacify the intermittency of the renewables, the wind-PV HRES has been promoted for delivering electricity to remote or islanded areas within the past two decades [3]. Compared with the conventional sole-wind or sole-solar energy generation, this HRES can achieve complementary daily and annual power patterns between the WECS and PV generation system. This leads to (i) smoothed net power generation of the HRES, (ii) improved space utilization rate, (iii) reduced installation cost, and (iv) prolonged lifetime of the energy storage system (ESS) [4]. However, with the expanding proportion of HRES, it is foreseeable that the stability of the utility grid, especially for the low-voltage distribution grid, will be compromised when grid faults occur [5]. In view of this, sufficient LVRT capability of the HRES is necessarily required by various grid codes for assisting the generators to survive the faults. Specifically, power electronic inverters are requested to operate with the grid-forming functionalities [6]. Typical LVRT operation criterions are summarized as shown in Fig. 1 [7]. As illustrated in Fig. 1(a), the generators are required to maintain connection with the main grid in case of voltage-dip circumstances above the borderlines. Meanwhile, corresponding reactive current is required to be provided based on the voltage sag depth at the point of common coupling (PCC) as shown in Fig. 1(b).

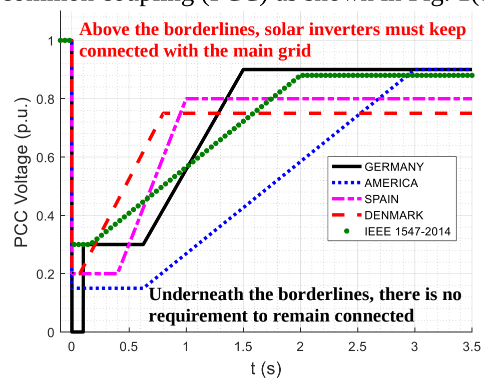

(a) LVRT operation criterions. (Without prejudice to generality, the strictest German grid code is adopted in this work.)

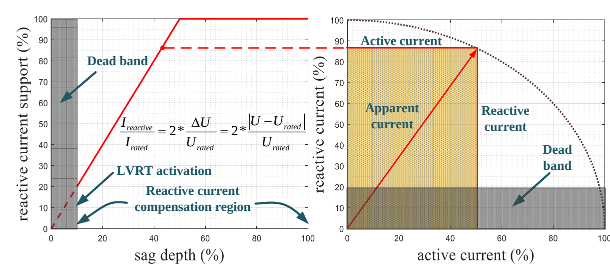

(b) Reactive current support. (When the voltage dip exceeds the dead zone, 2% of reactive current injected to the grid is commonly required for every 1% of PCC voltage dip.)

Fig. 1. Various LVRT grid codes on the distributed renewable energy system.

A. Related Works

Many studies have been conducted on achieving a satisfactory LVRT performance under the grid faults [6]-[24]. Recent LVRT strategies generally follow the stereotype of separating the energy balancing control and the reactive power compensation in a decoupled coordinate system. The decoupled inverter output current control is reported in [8], [9] to generate the required reactive current compensation in the synchronous

This work is supported by Research Grants Council (RGC) of Hong Kong, under Theme-based Research Scheme through Grant T23-701/14N. Y. F. He, M. H. Wang, and Z. Xu are with Department of Electrical Engineering in The Hong Kong Polytechnic University. (e-mails: 3120100780hyf@gmail.com; mhwang@polyu.edu.hk; zhao.xu@polyu.edu.hk).

rotating coordinate system. Symmetrical component method [10], direct power control (DPC) [11] and model predictive control (MPC) [12] have been adopted to decouple the control of active and reactive power output of the grid-connected inverters. Due to the operational limitations, the grid-tied active power must be reduced to avoid overvoltage and overcurrent in the system. To further extend the active power controllability of the renewable generation systems, crowbar circuits [13], braking resistors [14] and DC-choppers [15], [16] are widely applied for the LVRT operation of PMSG and PV systems. These methods are of low efficiency since the renewable energy are deliberately dissipated as heat for fulfilling the operational constraints. To avoid the energy dissipation, ESS (e.g. super capacitors and batteries) are applied for buffering the energy mismatch during the LVRT periods [17], [18]. However, the aforementioned energy management methods demand extra circuit components, which incurs implementation and maintenance costs. The renewable power curtailment methods of switching the generator-side converter to the non-maximum power point tracking (non-MPPT) operation are introduced in [19]. In order to improve the overall energy conversion efficiency of renewable energy generation and accelerate the post-fault recovery, the energy buffering capabilities of DC-Link capacitors [7] and the rotating mass [12], [20] are exploited in the PV and WECS system, respectively.

At present, few works on enhancing the LVRT capability of the wind-PV HRES have been reported [21]-[24]. In [21], [22], the crowbar circuit and the de-loading method are individually activated for the wind and solar farms. Solar PV string inverters are utilized as STATCOMs in the wind-PV HRES [23] only for providing reactive power compensation in the voltage transients. In [24], dynamic voltage restorer (DVR) is implemented for the HRES to improve the LVRT capability with external circuits.

B. Main Contribution

In the review of the existing LVRT control strategies of the HRES, the coordination between the WCES and the PV system is extremely weak, which leads to the suboptimal utilization of the embedded assets. Since the real power has a significant effect on the local power supply, the voltage support in the distribution network and power recovery acceleration after fault clearance [25], the active power regulation must be further discussed in the LVRT operation. Besides, the previous research for the HRES still lacks consideration about LVRT control under different environmental conditions.

In this paper, a novel coordinative LVRT control scheme is proposed for the wind-PV HRES. It distinguishes itself from the other reported methods with the following advantages:

- Energy harvesting is optimized in the LVRT operation. Specifically, certain renewable energy will be stored in the rotating mass and the DC-Link capacitor, which leads to an improved energy conversion efficiency. In the meantime, the safety constraints of the generation system and specified reactive current injection (RCI) as per the grid code are both satisfied. After fault clearance, the stored energy will be released to the grid for assisting the post-fault recovery.
- The designed controller is pro-active to different environmental conditions and voltage dips. Four different controllers, which are for the DC-Link voltage control, PMSG rotating speed control, PV power curtailment control, and blade pitch angle control, are deployed to cope with different operating conditions and faults for achieving the full use of system energy inertia and optimizing the renewable energy harvesting.
- Direct output control, which is with an adjustable DC-Link control structure, is proposed for the wind-PV HRES, which can achieve the accurate and stable current output of the grid-side converter (GSC) during faults.

This paper is organized as follows: In Section II, the wind-PV HRES is introduced. In Section III, the proposed coordinative control scheme for enhancing the LVRT capability of the HRES is elaborated. The optimization principles and different control modes are discussed. In Section IV, the HIL experimental results based on the Digital Signal Processing and Control Engineering (dSPACE) are provided to verify the functionality of the proposed LVRT control scheme. In Section V, the simulation results are provided for comparing the performances of the proposed and conventional LVRT methods.

II. The Wind-PV HRES in the DC-shunt Topology

In this work, the PMSG-based wind turbine (WT) is adopted instead of the doubly-fed induction generator (DFIG), since (i) the industrial implementation of PMSG-based offshore wind farms is increasing, and (ii) the DC-Link capacitor in the PMSG-based WECS is larger than that in the DFIG-based WECS, which improves the energy buffering capacity for the LVRT operation. The model of the PMSG can be plotted in Fig. 2. It consists of the wind generation model, the permanent magnet synchronous machine (PMSM) and the three-phase controlled full-bridge rectifier.

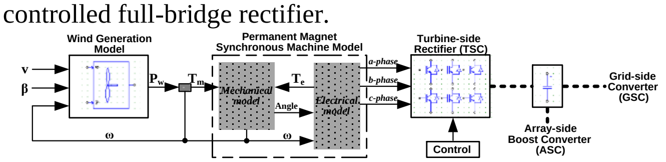

Fig. 2. PMSG model diagram.

The DC-shunt connection of the HRES, where the PMSG and the PV arrays are coupled at the DC bus, is becoming popular in the state-of-the-art research due to the ease of integration and the absence of power quality issues [26]. The layout of this wind-PV HRES is plotted in Fig. 2 and Fig. 3(a), where the PMSG and PV arrays are connected to a common DC-link capacitor through the turbine-side converter (TSC) and array-side converter (ASC), respectively. The DC-Link is connected to the utility grid through a three-phase GSC and a step-up transformer.

Normally, the wind-PV HRES is for generating the consistent and reliable electric power to the remote/islanded areas [26], where the system is usually connected with the low-voltage distribution network (LVDN) [5]. In this application, it is proved that the active current output of the GSC will have a significant influence on the voltage support since the resistive component of the line impedance is non-negligible [27]. In addition, the sufficient local power supply in the fault and a rapid active power recovery rate after the fault clearance are recommended in the grid code [25]. Therefore, in this work, the energy harvesting and the active current injection are prioritized after fulfilling the specified RCI based on the grid code requirements.

III. Proposed Coordinative LVRT Control Scheme for the Wind-PV Hybrid System

The overall block diagram of the proposed coordinative LVRT control scheme is illustrated in Fig. 3(b). Embedded energy management controllers, which will be introduced in Subsection III.A, are coordinated in the proposed LVRT operation. Direct output control will be proposed for ensuring the accurate and stable output current regulation in Subsection III.B. After the fault is detected, the supervisory LVRT controller optimizer will determine the optimized control mode and structure based on the working conditions, which will be further discussed in Subsection III.C.

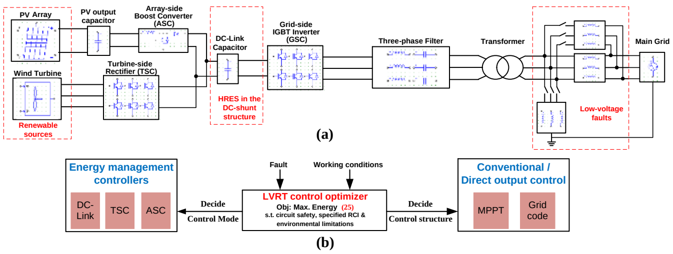

Fig. 3. (a) Wind-PV HRES in the DC-shunt topology. (b) The overall diagram of the proposed coordinative LVRT control scheme.

A. *Available Controllers for Safe LVRT Process and Energy Management*

When a PCC voltage dip occurs, the harvested excessive energy will lead to overvoltage or overcurrent circumstances in the system. To avoid this, the renewable generation is generally stored or curtailed for the safe operation of the system. To boost the energy conversion efficiency, the adaptive DC-Link voltage controller and the PMSG rotating kinetic energy controller can be applied to enable an active power buffering of the DC-Link capacitor and the rotor mass. To avoid the renewables over-energizing the HRES, the PMSG rotating kinetic energy controller, the PV power curtailment controller and the PMSG blade pitch angle controller can be used to curtail the renewable power output during faults.

1) Adaptive DC-Link Voltage Controller

Different from the conventional LVRT control scheme, where the DC-Link voltage u_{dc} is regulated to a constant value of 1 p.u., the proposed control scheme will adaptively operate u_{dc} for buffering the power imbalance between the DC and AC terminals. By the Law of Energy Conservation, the dynamic of u_{dc} can be described as

$$Cu_{dc}\frac{du_{dc}}{dt} = p_{pv} + p_{pmsg} - p_g \tag{1}$$

where C is the DC-Link capacitance. p_{pv}, p_{pmsg} and p_g are the instantaneous power of the ASC output, the TSC output and the power transmitted to the GSC, respectively.

In the determination of the voltage rating of the DC-Link capacitors, a design margin of 30-50% is preserved due to the reliability and security concerns of the grid-forming GSC [28]. In view of this, in the proposed adaptive DC-Link voltage control, the DC-Link voltage reference during the LVRT period U_{dcref}^{lvrt} can be temporarily higher than the nominal value for storing certain energy in the DC-Link capacitors. The stored energy E_{cap}^{store} can be expressed as

$$E_{cap}^{store} = \frac{1}{2}C\cdot(U_{dcref}^{lvrt\ 2} - U_{dcref}^{norm2}) = K\cdot t_p(P_{rated} - P_{gref}) \tag{2}$$

where t_p is the hold-up time of LVRT operation as per grid codes. U_{dcref}^{norm} is the nominal voltage of the DC-Link capacitor. P_{rated} is the rated power output of the GSC in normal operation. P_{gref} is the theoretical output power of GSC in the LVRT operation, which is essentially the maximum allowable real power output of the GSC with respect to the specific PCC voltage fault. K is the slack coefficient to regulate the percentage of extra energy stored in the capacitors. By (2), U_{dcref}^{lvrt} can be calculated by using

$$U_{dcref}^{lvrt} = \sqrt{U_{dcref}^{norm2} + \frac{2\cdot t_p(P_{rated} - P_{gref})\cdot K}{C}} \tag{3}$$

The overvoltage circumstance can be avoided by choosing a proper K. It should be noted that U_{dcref}^{lvrt} is bounded by the voltage limits of both the DC-Link capacitors and the active switches. In comparisons with the conventional LVRT strategies in the fault, certain renewable energy can be stored without any additional components involved and the renewable energy curtailment can be accordingly realized.

Once the fault is cleared, the U_{dcref} will be restored to the nominal value, and the stored energy will be released to the grid. Considering the MPPT algorithm is usually of slow dynamic, this immediate release of the stored energy in the DC-Link capacitors will potentially speed up the recovery of active power output and improve the resilience of the power system.

2) PMSG Rotating Kinetic Energy (KE) Controller

In case of the voltage dip, it is desirable to store certain extra energy as the KE of the rotating mass by accelerating the rotor of the PMSG, as shown in Fig. 4(a). When the fault happens, the PMSG can temporarily increase the rotor speed to transform the wind energy into the KE. When the fault is cleared, the stored energy in the rotor will be transferred to the grid via the TSC, and the rotating speed is restored to the MPP. In the meantime, this acceleration can curtail the output power generation of the PMSG. The dynamic of the rotating speed can be expressed as,

$$2H\omega\frac{d\omega}{dt} = P_m - P_e \tag{4}$$

where P_m and P_e are the mechanical power and electromagnetic power of the WT generator, respectively. H denotes the inertia time constant of PMSG, which can be defined in (5),

$$H = \frac{J\omega_n^2}{2P_n} \quad J = J_t + J_g \tag{5}$$

where P_n and ω_n are the nominal power output and rotating speed of the PMSG, respectively. J represents the joint inertia that is the sum of the turbine inertia J_t and the generator inertia J_g.

It is reported that the effective rotor acceleration can be achieved during the fault period [9], [30]. Besides, the wind-PV HRES is usually connected to the distributed networks [5]. Its power capacity is usually of the hundred-kW, which leads to a relatively small inertia. Therefore, with the proposed control, the HRES will firstly reduce the output power of TSC rather than the power curtailment of ASC so that a considerable amount of energy E_{pmsg}^{store} will be stored in the rotor. The correlation between E_{pmsg}^{store} and the rotating speed is described in (6), where ω_{lvrt} and ω_{norm} represent the rotor speed in the LVRT and normal operation, respectively.

$$E_{pmsg}^{store} \propto \Delta\omega^2 \propto \omega_{lvrt}^2 - \omega_{norm}^2 \tag{6}$$

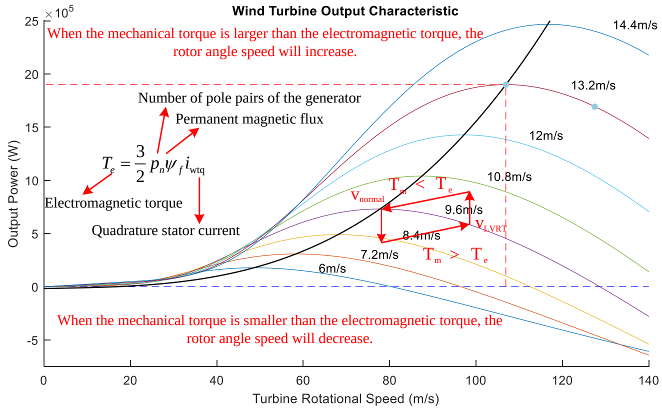

(a)

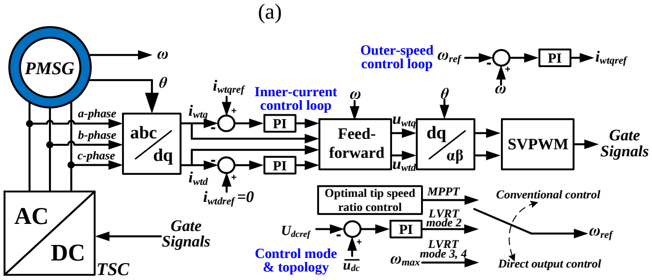

(b)

Fig. 4. (a) Wind turbine output characteristic. (b) TSC control block diagram.

As illustrated in Fig. 4(b), in the normal operation, the rotating speed reference ω_{ref} is determined by the MPPT algorithm. During the fault, ω_{ref} is determined by a supervisory LVRT control optimizer, which will be discussed later. The TSC is controlled in the synchronous rotating (d-q) coordinate system. Here, the inner-current control loops are adopted to control the output current of the PMSG. The d-axis current i_{wtdref} is aligned with the rotor flux direction, which is consistently regulated at zero. Since the q-axis current is approximately linearly related to the electromagnetic torque, the q-axis current reference i_{wtqref} is generated by the outer-speed control loop, which can be expressed as

$$i_{wtqref} = (\omega - \omega_{ref}) \cdot (KP_{\omega} + \frac{KI_{\omega}}{s}) \tag{7}$$

where KP_{ω} and KI_{ω} denote the proportional and integral parameters of the PI compensator, respectively. Correspondingly, the duty ratios of u_{wtd} and u_{wtq} in the d-q frame can be obtained by using

$$u_{wtq} = (i_{wtq} - i_{wtqref}) \cdot (KP_{wtq} + \frac{KI_{wtq}}{s}) + \omega\psi_f + L\omega i_{wtd} \tag{8}$$

$$u_{wtd} = (i_{wtd} - i_{wtdref}) \cdot (KP_{wtd} + \frac{KI_{wtd}}{s}) - L\omega i_{wtq} \tag{9}$$

where i_{wtd} and i_{wtq} are the stator current in the d-q frame. L is the inductance. Ψ_f is the magnetic flux. KP_{wtd}, KI_{wtd}, KP_{wtq}, and KI_{wtq} denote the PI parameters.

As shown in Fig. 4(a), when power curtailment is required in the LVRT period, ω_{ref} will be increased to accelerate the rotor, which will reduce the power generation of the TSC. In the meantime, a considerable amount of wind energy can be stored as the KE of the rotor.

3) *PV Power Curtailment Controller*

In normal operation, the P&O MPPT algorithm is applied to generate the PV output current reference i_{pvref}. A PI compensator is applied for regulating output current of the PV array i_{pv} to i_{pvref}, i.e.

$$d_{pv} = (i_{pv} - i_{pvref}) \cdot (KP_{pv} + \frac{KI_{pv}}{s}) \tag{10}$$

where d_{pv} is the duty ratio of the ASC. KP_{pv} and KI_{pv} are the proportional and integral gains of the PI controller, respectively.

When the operating voltage exceeds the MPP, the output power of the PV array is positively correlated with the PV output current. Hence, if PV output curtailment is required during the PCC voltage fault period, the PV output current will be regulated below the MPP, as shown in Fig. 5. Since the curtailed energy cannot be stored in the PV array, the PMSG will be firstly engaged in the power curtailment during the LVRT operation rather than the PV array. In this way, more renewable energy can be stored and utilized to assist the power recovery after the fault clearance.

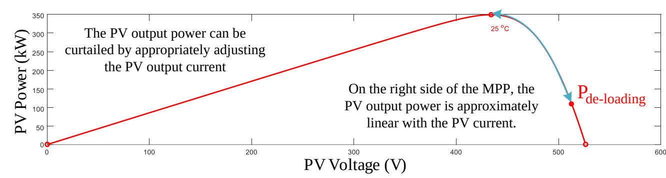

Fig. 5. PV power curtailment control in the LVRT period.

4) *PMSG Blade Pitch Angle Controller*

In case of a severe voltage dip limiting the power transferring capacity of the GSC, the pitch angle controller of the PMSG will be activated to mechanically curtail the harvested wind energy and guarantee a safe LVRT process of the HRES. The block diagram of the pitch angle control is plotted in Fig. 6. The pitch angle is limited within 0 º to 90 º, and its ramping rate is set to be $\pm 8^o/s$ [29].

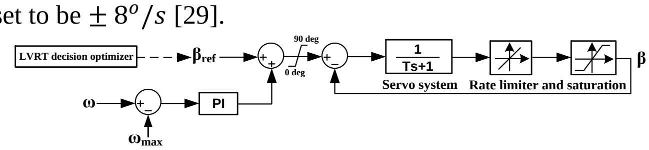

Fig. 6. Block diagram of pitch angle controller.

After detecting a severe voltage dip, the LVRT control optimizer will regulate the pitch angle to a positive value for curtailing the harvested wind energy. Considering that this control approach renders irreversible energy losses and is slower than the rotating speed control, it will be only activated when all the aforementioned control approaches have fully exploited the available energy buffering capacity of the HRES.

B. *Direct output control*

In order to accurately regulate the GSC output current during the grid faults, a direct output control method is proposed, as illustrated in Fig. 7.

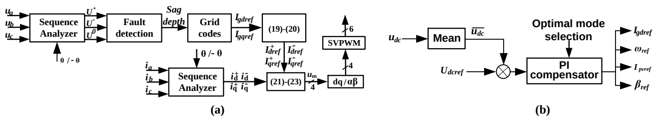

Fig. 7. Block diagrams of the direct output control for (a) the GSC. (b) the DC-Link voltage.

1) Derivation of Active and Reactive Current References

For the unbalanced voltage sag, the grid voltage $\boldsymbol{u_{abc}} = [\,u_a\ u_b\ u_c]^T$ can be decomposed into positive-sequence voltage $\boldsymbol{u^+_{abc}}$, negative-sequence voltage $\boldsymbol{u^-_{abc}}$ and zero-sequence voltage $\boldsymbol{u^0_{abc}}$, i.e.,

$$\mathbf{u}_{abc} = \mathbf{u}^{+}_{abc} + \mathbf{u}^{-}_{abc} + \mathbf{u}^{0}_{abc} = U^{+}\begin{bmatrix}\sin(\omega t+\theta^{+})\\ \sin(\omega t-2\pi/3+\theta^{+})\\ \sin(\omega t+2\pi/3+\theta^{+})\end{bmatrix} + U^{-}\begin{bmatrix}\sin(\omega t+\theta^{-})\\ \sin(\omega t+2\pi/3+\theta^{-})\\ \sin(\omega t-2\pi/3+\theta^{-})\end{bmatrix} + U^{0}\begin{bmatrix}\sin(\omega t+\theta^{0})\\ \sin(\omega t+\theta^{0})\\ \sin(\omega t+\theta^{0})\end{bmatrix} \quad (11)$$

where U^+, U^- and U^0 denote the amplitude of the positive-, negative- and zero-sequence components, respectively. θ^+, θ^- and θ^0 denote the corresponding initial phase angles. Similarly, for the grid-tied current of GSC $\boldsymbol{i_{abc}} = [\,i_a\ i_b\ i_c]^T$, it can be derived that

$$\mathbf{i}_{abc} = \mathbf{i}^{+}_{abc} + \mathbf{i}^{-}_{abc} + \mathbf{i}^{0}_{abc} \quad (12)$$

where $\boldsymbol{i^+_{abc}}$, $\boldsymbol{i^-_{abc}}$ and $\boldsymbol{i^0_{abc}}$ denote the positive-, negative- and zero-sequence current vectors, respectively.

In three-phase-three-wire system, $\boldsymbol{i^0_{abc}}$ is always zero. According to the instantaneous power theory [31], the instantaneous real power p_i and imaginary power q_i can be expressed as

$$\begin{bmatrix}p_i\\ q_i\end{bmatrix} = \begin{bmatrix}u_a i_a + u_b i_b + u_c i_c\\ \frac{1}{\sqrt{3}}[(u_a-u_b)i_c + (u_b-u_c)i_a + (u_c-u_a)i_b]\end{bmatrix} = \begin{bmatrix}\overline{P} + P_c\cos(2\omega t) + P_s\sin(2\omega t)\\ \overline{Q} + Q_c\cos(2\omega t) + Q_s\sin(2\omega t)\end{bmatrix} \quad (13)$$

where $\bar{P}$ and $\bar{Q}$ denote the average active and reactive power outputs of the GSC. P_c, P_s, Q_c and Q_s denote the pulsating powers. In the synchronous rotating frame, the power components in (13) can be expressed as

$$\begin{bmatrix}\overline{P}\\ \overline{Q}\\ P_c\\ P_s\\ Q_c\\ Q_s\end{bmatrix} = \frac{3}{2}\begin{bmatrix}u_d^+ & u_q^+ & u_d^- & u_q^-\\ u_q^+ & -u_d^+ & u_q^- & -u_d^-\\ u_d^- & u_q^- & u_d^+ & u_q^+\\ u_q^- & -u_d^- & -u_q^+ & u_d^+\\ u_q^- & -u_d^- & u_q^+ & -u_d^+\\ -u_d^- & -u_q^- & u_d^+ & u_q^+\end{bmatrix}\begin{bmatrix}i_d^+\\ i_q^+\\ i_d^-\\ i_q^-\end{bmatrix} \quad (14)$$

where u_d^+, u_q^+, u_d^-, and u_q^- denote the sequential d-q components of PCC voltage. Similarly, i_d^+, i_q^+, i_d^-, and i_q^- denote the corresponding components of the current injected to the grid.

It can be observed in (14) that there are only four free variables can be independently controlled. As the negative-sequence current can result in the opposite magnetic field and the asymmetrical load current, which is unacceptable by the Transmission System Operator (TSO) [25], it is desirable to set the control references of negative-sequence current I^-_{dref} and I^-_{qref} at zero, i.e.,

$$I^-_{dref} = 0 \quad I^-_{qref} = 0 \quad (15)$$

In the unbalanced system, the voltage sag depth can be defined as,

$$U_{sag} = |U_{rated} - \frac{U^+}{\sqrt{2}}| = |U_{rated} - \sqrt{\frac{(U_d^+)^2 + (U_q^+)^2}{2}}| \quad (16)$$

where U_{rated} is the rated PCC RMS voltage. U_d^+ and U_q^+ are the RMS values of u_d^+ and u_q^+, respectively.

According to the grid code, if the PCC voltage sag U_{sag} is larger than 10% of U_{rated}, 2% of reactive current I^{lvrt}_{gqref} must be generated per 1% of voltage sag, which can be described as

$$I^{lvrt}_{gqref} = 2\cdot\frac{U_{sag}}{U_{rated}}\cdot I_{rated} \quad (17)$$

where I_{rated} is the RMS value of the GSC rated output current.

During the fault, the active power still needs to be generated for maintaining local loads and potentially supporting the PCC voltage in the LVDN. To convert as much renewable energy as possible from the HRES to the grid during the fault, the power electronic components can be temporarily operated above the rated value for achieving a larger power transferring capacity. In this paper, the apparent current of GSC is temporarily set to be 1.1 p. u. during faults as illustrated in Fig. 8. Consequently, the upper bound of the active current output of the GSC I^{lvrt}_{gdref} can be calculated as

$$I^{lvrt}_{gdref} = \sqrt{(1.1\cdot I_{rated})^2 - I^{lvrt\ 2}_{gqref}} \quad (18)$$

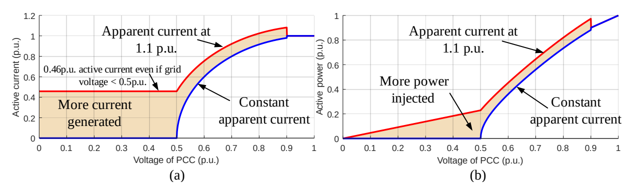

Fig. 8. (a) Current-voltage and (b) power-voltage operating curves of the GSC.

In order to provide the required active and reactive power to the grid, the active and reactive current references (i.e., I_{gdref} and I_{gqref}) should satisfy that

$$\overline{P} = \frac{3}{2}\cdot U^+\cdot I_{gdref} \qquad \overline{Q} = \frac{3}{2}\cdot U^+\cdot I_{gqref} \quad (19)$$

By substituting (15) and (19) into (14), it can be derived that

$$\begin{bmatrix}I^+_{dref}\\ I^+_{qref}\end{bmatrix} = \frac{2}{3}\begin{bmatrix}\dfrac{u_d^+\cdot\overline{P} + u_q^+\overline{Q}}{(u_d^+)^2 + (u_q^+)^2}\\ \dfrac{u_q^+\cdot\overline{P} - u_d^+\overline{Q}}{(u_d^+)^2 + (u_q^+)^2}\end{bmatrix} \quad (20)$$

By applying the current references calculated by (15) and (20), the three-phase output current of the GSC will be controlled to be balanced and symmetrical since only positive-sequence components of the current exist both in the normal and LVRT operation. Besides, the double-line-frequency pulsating power induced in the asymmetrical voltage fault condition will be buffered by the DC-Link capacitors.

2) Direct output control under Grid Faults

For the conventional LVRT control strategies, the referenced value of the GSC active current I_{dref}^{+} is generated by the DC-Link voltage controller [8]. In the meantime, the referenced power of TSC/ASC is mathematically calculated as illustrated in Fig. 9 (see the blue arrows). It does not take the power losses of the converters (which is around 5%-10%) into account. Inevitably, this will result in the power injection to the grid always being lower than the calculated renewable power reference. Furthermore, due to the imperfect modeling of the HRES, it is difficult to accurately determine the respective power references for the PV arrays and wind turbines through this open-loop mathematical calculation.

To resolve these problems, the direct output control, which will directly regulate the positive and negative-sequence components of GSC output current i_d^+, i_q^+, i_d^- and i_q^- with their own single-PI control loops, is proposed as shown in Fig. 7(a). Based on the dynamic characteristics of the GSC, the control signals of positive or negative sequential components can be obtained for achieving the decoupled control, i.e.,

$$\begin{aligned}\begin{bmatrix} u_{md}^{+} \\ u_{mq}^{+} \end{bmatrix} &= \begin{bmatrix} u_{d}^{+} \\ u_{q}^{+} \end{bmatrix} + \begin{bmatrix} k_{pi}^{+d} & 0 \\ 0 & k_{pi}^{+q} \end{bmatrix} \begin{bmatrix} I_{dref}^{+} \\ I_{qref}^{+} \end{bmatrix} \\ &+ \begin{bmatrix} -k_{pi}^{+d} + R_i & -\omega_g L_i \\ \omega_g L_i & -k_{pi}^{+q} + R_i \end{bmatrix} \begin{bmatrix} i_{d}^{+} \\ i_{q}^{+} \end{bmatrix}\end{aligned} \tag{21}$$

$$\begin{aligned}\begin{bmatrix} u_{md}^{-} \\ u_{mq}^{-} \end{bmatrix} &= \begin{bmatrix} u_{d}^{-} \\ u_{q}^{-} \end{bmatrix} + \begin{bmatrix} k_{pi}^{-d} & 0 \\ 0 & k_{pi}^{-q} \end{bmatrix} \begin{bmatrix} I_{dref}^{-} \\ I_{qref}^{-} \end{bmatrix} \\ &+ \begin{bmatrix} -k_{pi}^{-d} + R_i & \omega_g L_i \\ -\omega_g L_i & -k_{pi}^{-q} + R_i \end{bmatrix} \begin{bmatrix} i_{d}^{-} \\ i_{q}^{-} \end{bmatrix}\end{aligned} \tag{22}$$

$$k_{pi}^{\pm d,q} = K_1 P_{\pm d,q} + \frac{K_2 I_{\pm d,q}}{s} \tag{23}$$

where u_{md}^+, u_{mq}^+, u_{md}^- and u_{mq}^- are the duty ratios in the d-q frame. ω_g is fundamental frequency of the system, L_i and R_i are the inductance and resistance of the filter, respectively. k_{pi}^{+d}, k_{pi}^{+q}, k_{pi}^{-d} and k_{pi}^{-q} denote the parameters of PI compensators of the current control loops. The duty ratios will then be projected onto the α-β frame for implementing the space vector pulse width modulation (SVPWM) of the GSC. Different from the conventional control, the I_{dref}^+, I_{qref}^+, I_{dref}^- and I_{qref}^- are directly calculated based on the grid code and circuit operational limits, as shown in (15)-(20).

The dynamic of the GSC output current error $e_{d/q}^{+/-}$ can be designed to converge from its initial value $e(0)$ to zero as

$$e_{i\_d/q}^{+/-}(s) = \frac{sL_i e(0)}{L_i s^2 + K_1 s + K_2} \tag{24}$$

By applying the loop-shaping method, coefficients K_1 and K_2 can be determined based on the switching frequency and system parameters.

As described in (1), the DC-Link voltage variation reflects the power imbalance between the PV & PMSG power output and the GSC power input. In the direct output control, depending on the selected control mode, the DC-Link voltage controller will be operated to generate the referenced rotating speed of the PMSG, the referenced current of the PV array or the referenced pitch angle, as shown in Fig. 7(b).

There are two advantages about this direct output control, namely, (i) As illustrated in Fig. 9, the DC-Link voltage control loop will automatically compensate for the power loss amidst the energy conversion process from the renewables to the grid. The intermediate benefit is the enhanced controllability of the system and improved energy efficiency since a certain amount of renewable generation is harvested for compensating for the conversion loss. (ii) The direct derivation and implementation of the current references of the GSC can lead to the accurate and stable output current control.

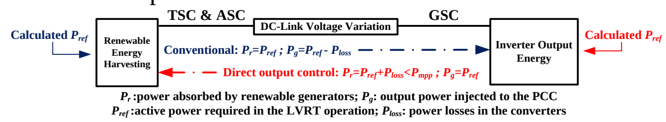

Fig. 9. Illustration of HRES power flows with the proposed direct output control and the conventional control.

C. LVRT Control Optimizer with Adjustable Control Structures

The voltage sag induced by the faults will decrease the power transferring capacity of the GSC, which congests the power delivery of the renewables. To manage the energy flows of the HRES and achieve a higher energy efficiency with respect to different environmental factors (e.g., wind speed, solar irradiance, and temperature), an LVRT decision optimizer is proposed for maximizing the harvested energy under the premise of ensuring the circuit safety and specified RCI throughout the LVRT operation. Besides, a certain amount of renewable energy can be reserved in DC-Link capacitors and the PMSG rotating mass, which will be released after fault clearance to accelerate the post-fault recovery. The formulation of the LVRT optimizer can be expressed as

$$z = \begin{bmatrix} I_{pvref} & \omega_{ref} & \beta_{ref} & U_{dcref} & I_{gdref} & I_{gqref} \end{bmatrix}^T \tag{25.a}$$

$$Obj: \quad \underset{z}{\arg\max} \; E_{pv} + E_{pmsg} \tag{25.b}$$

$$subject\ to \quad P_{pv} \le P_{pv}^{*},\ P_{pmsg} \le P_{pmsg}^{*} \tag{25.c}$$

$$0 \le I_{pvref} \le I_{pv}^{*} \tag{25.d}$$

$$\omega^{*} \le \omega_{ref} \le \omega_{max},\ 0 \le \beta_{ref} \le \beta_{max} \tag{25.e}$$

$$I_{gqref} \ge I_{gqref}^{lvrt},\ I_{gdref} \le I_{gdref}^{lvrt} \tag{25.f}$$

$$U_{dcref}^{norm} \le U_{dcref} \le U_{dcref}^{lvrt} \tag{25.g}$$

In (25.b), E_{pv} and E_{pmsg} denote the energy harvested by the PMSG and PV arrays during the fault, respectively. Equivalently, it can be reformulated as

$$max. \int_0^{T_{fault}} P_g \cdot dt + E_{pmsg}^{store} + E_{cap}^{store} \tag{26}$$

As shown in (26), in order to maximize the harvested renewable energy during the fault, it is feasible to (i) inject the active power P_g to the grid at its maximum permissive rate in the specific voltage fault, (ii) actively engage the capacitive storage E_{cap}^{store} for buffering certain excessive renewable generation, and (iii) make full use of the rotor inertia to store the wind power in the form of kinetic energy E_{pmsg}^{store}.

The LVRT optimizer will generate the optimal references (i.e. decision variable z), which includes control references of PV current I_{pvref}, PMSG rotor speed ω_{ref}, pitch angle β_{ref}, DC-Link voltage U_{dcref}, active current I_{gdref} and reactive current I_{gqref} of the GSC in the LVRT operation. ω_{max} and β_{max} are the maximum allowable rotating speed and pitch angle of the PMSG, respectively. P_{pv}^{*}, I_{pv}^{*}, P_{pmsg}^{*}, and ω^{*} are the PV output power and current, PMSG output power and rotating speed, respectively, at the fault instant, when the HRES is still with the MPPT control in normal operation. Practically, the sum of P_{pv}^{*} and P_{pmsg}^{*} is usually smaller than the rated power of the GSC, i.e.,

$$P_{gnom} = P_{pv}^{*} + P_{pmsg}^{*} \le P_{rated} = 3 \cdot U_{rated} \cdot I_{rated} \tag{27}$$

$P_{\omega max}^{*}$ is the power generated by the PMSG when the rotating speed is close to ω_{max}. Considering the fault duration T_{fault} is relatively short, e.g. several hundreds of milliseconds or a few seconds, it can be assumed that the environmental condition does not change during T_{fault}. Consequently, the maximum allowable active power P_{gref} injected to the grid during the fault can be derived as

$$P_{gref} = \frac{3}{2} U^{+} \sqrt{(1.1 \cdot I_{rated})^2 - I_{gqref}^{lvrt\ 2}} \tag{28}$$

The proposed solution is illustrated in Fig. 10 and Table I of the Appendix, which can be further explained in four modes with self-adjustable control structures as follows:

(i) **When $P_{gref} \ge P_{pmsg}^{*} + P_{pv}^{*}$,** the TSC and ASC will still be operated with the MPPT control. In this mode, the power flows in the HRES are inherently balanced, and all the renewable energy is injected to the grid.

(ii) **When $P_{\omega max}^{*} + P_{pv}^{*} \le P_{gref} < P_{pmsg}^{*} + P_{pv}^{*}$,** the power flow from the renewables to the grid is congested. The PMSG rotor will be accelerated so that certain wind energy will be stored as the kinetic energy in a regenerative manner. Since the excessive energy is completely buffered by the rotor, the PV array can be operated in the MPPT mode. Compared with the conventional control scheme, the unnecessary curtailment of the PV generation is avoided, which improves the energy efficiency. In the meantime, the direct output control is activated in this mode. ω_{ref} will be generated by the DC-Link voltage controller.

(iii) **When $P_{\omega max}^{*} \le P_{gref} < P_{\omega max}^{*} + P_{pv}^{*}$,** the PMSG will be operated at the maximum rotating speed ω_{max}. Since all the energy storage capability has been exploited, the PV output power will be curtailed for the system safety. The DC-Link voltage controller is switched to generate required I_{pvref}.

(iv) **When $0 < P_{gref} < P_{\omega max}^{*}$,** the system will have to mechanically curtail the energy harvesting with the pitch angle control. In this mode, the PV power generation is ceased, while the PMSG is operated at the maximum rotating speed. The DC-Link voltage controller is switched to generate required β_{ref}.

Besides, in every control mode, the average voltage of DC-Link capacitors will be increased to store certain extra energy as the electrical potential energy, which can increase the energy harvesting and accelerate the post-fault power recovery. The specified reactive current based on the grid codes will be injected to the PCC. It is worthy of mentioning that compared with traditional separated control on the WT and PV systems without coordination, more renewable energy can be stored since the PV generator is only de-loaded when the PMSG rotor reaches ω_{max}.

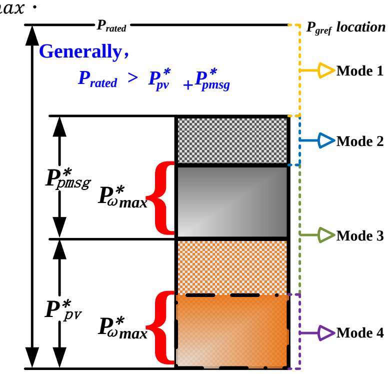

Fig. 10. Control mode selection according to the P_{gref} location.

The flow chart of the proposed LVRT control scheme can be plotted as shown in Fig. 11. When the fault is detected, the system conditions at the fault instant will be recorded. Then the LVRT decision optimizer will immediately determine the optimized control mode and restructure the controllers according to the voltage sag depth and system condition records. The corresponding references will be calculated for the LVRT operation based on the grid codes and circuit operational limitations.

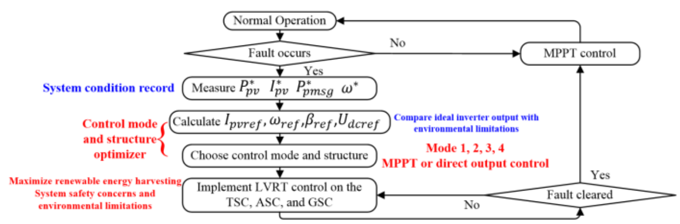

Fig. 11. Flow chart of the proposed coordinative LVRT control.

IV. HARDWARE-IN-THE-LOOP EXPERIMENTAL VALIDATION

To achieve the real-time (RT) emulation of the destructive grid faults and the responses in the large HRES, the HIL experiments are conducted based on the dSPACE. The configuration of the HIL test platform for validating the effectiveness of the proposed LVRT control can be plotted as shown in Fig. 12. The proposed control scheme is programmed in a commercialized DSP (TMSF28069, TEXAS INSTRUMENT). Its control signals (switching pulses) is fed back to the FPGA, which is programmed with the dynamics of the wind-PV HRES. The measurements of the wind-PV HRES are delivered to the DSP via analog output terminals of the dSPACE and A/D terminals of the DSP. The specifications of the experiment setup are provided in the Table II of the Appendix.

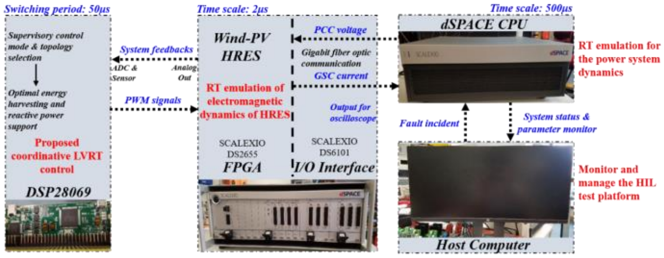

Fig. 12. dSPACE-based HIL.

A. *LVRT Control under the Three-Phase Symmetrical Voltage Sag with Various Environments*

The proposed coordinative control will effectively manage the embedded resources of the HRES with an optimized manner during the LVRT operation. Four experiments under three-phase symmetrical voltage dips of different severity are conducted with various wind speed *v* and solar irradiance *S*. The experimental waveforms are normalized and displayed as shown in Fig. 13-16.

In the first scenario, the wind speed and solar irradiance are set to be 10 m/s and 550 W/m^2, respectively. When the fault occurs, the PCC voltage drops from 1 p.u. to 0.8 p.u.. By calculation of the LVRT control optimizer, the renewable power generation will not over-energize the HRES under this slight voltage fault. Therefore, the PMSG and the PV array are still operated at the MPPs, as illustrated in Fig. 13. Meanwhile, the DC-Link voltage is increased from 1 p.u. to 1.05 p.u. for storing extra energy in the capacitors. After the fault is cleared, the electrical potential energy stored will be released, which can potentially accelerate the post-fault power recovery.

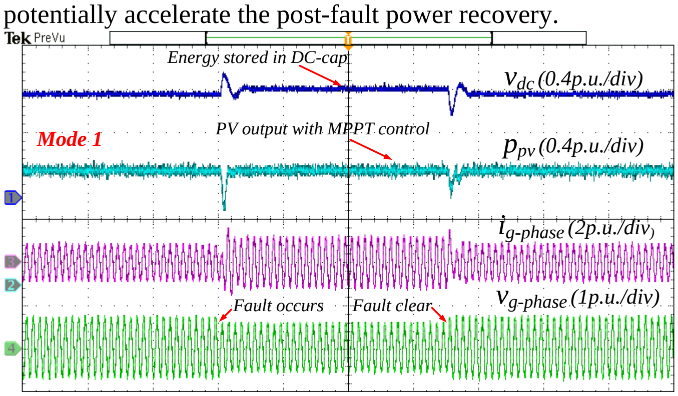

Fig. 13. *Waveform results of the DC-Link voltage, the rotor speed, the GSC phase current, and the GSC phase voltage*--Mode 1.

In the second scenario, the wind speed and the solar irradiance are 9 m/s and 850 W/m^2, respectively. When the PCC voltage drops from 1 p.u. to 0.65 p.u., LVRT control mode 2 will be selected by the optimizer since the PMSG has the sufficient capability for system safety. As illustrated in Fig. 14, the DC-Link voltage will be increased to 1.1 p.u. for storing extra energy in the capacitors. Meanwhile, the PMSG rotor is accelerated for curtailing the acquired wind power and simultaneously buffering the wind energy as the kinetic energy. With the direct output control, it can be derived that the GSC is delivering the apparent current of 1.1 p.u. and the reactive current of 0.7 p.u. to the grid during the fault. After the fault is cleared, the DC-Link voltage and rotor speed will be restored to the 1p.u., respectively.

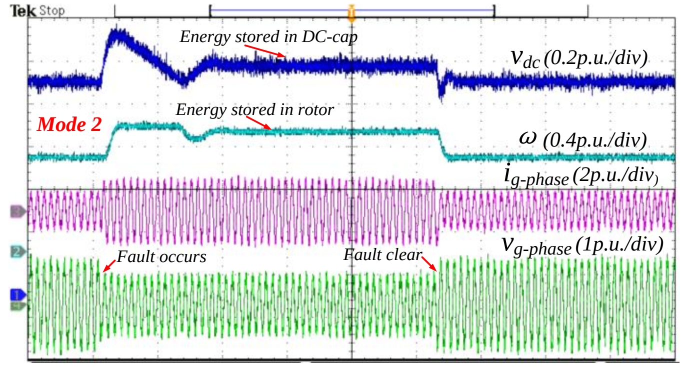

Fig. 14. *Waveform results of the DC-Link voltage, the rotor speed, the GSC phase current, and the GSC phase voltage*--Mode 2.

In the third scenario, when the PCC voltage drops from 1p.u. to 0.5 p.u., LVRT control mode 3 will be determined by the optimizer since all the energy buffering capability of the PMSG has been exploited. The rotor is accelerated to the ω_{max}. As illustrated in Fig. 15, the DC-Link voltage is increased from 1 p.u. to 1.1 p.u. for storing certain energy in the capacitors. The apparent output current of the GSC is increased from 0.45 p.u. with the MPPT control to 1.1 p.u. in the LVRT control. Meanwhile, the PV power generation is curtailed for the system safety. When the fault is cleared, the MPPT control will be resumed, and the DC-Link voltage will be restored to 1 p.u.

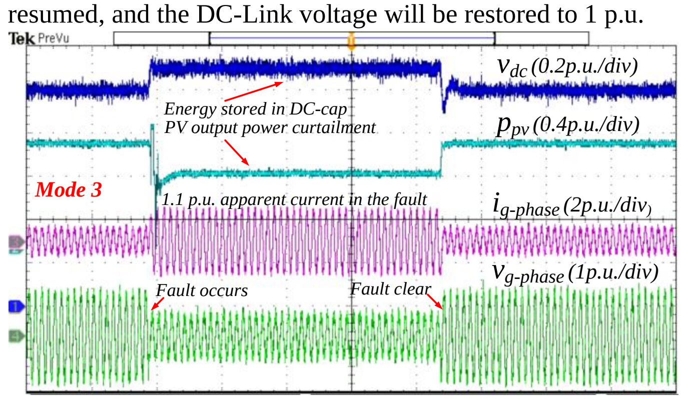

Fig. 15. *Waveform results of the DC-Link voltage, the PV power, the GSC phase current, and the GSC phase voltage* --Mode 3.

In the fourth scenario, the wind speed and solar irradiance are set to be 8 m/s and 800 W/m^2, respectively. When the fault occurs, the PCC voltage drops from 1 p.u. to 0.15 p.u.. Since the output power capacity is extremely small in this severe voltage dip, the LVRT control mode 4 is determined by the optimizer. The output power of the PV array is curtailed from 1 p.u. to 0 p.u., while the output power of the PMSG is mechanically curtailed to 0.2 p.u. in the fault, as illustrated in Fig. 16. Meanwhile, the GSC delivers the apparent current of 1.1 p.u. with the reactive current of 1 p.u. to the grid during the LVRT operation.

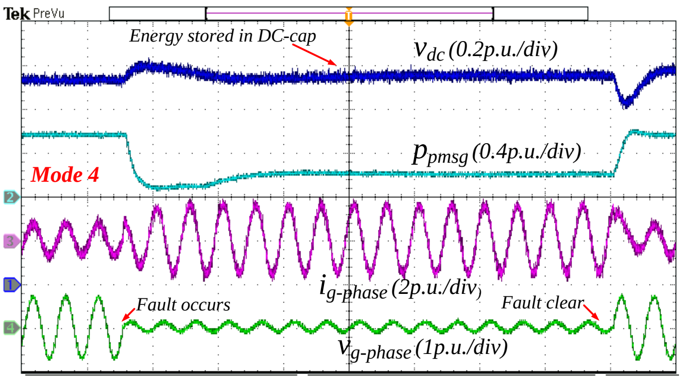

Fig. 16. *Waveform results of the DC-Link voltage, the rotor speed, the GSC phase current, and the GSC phase voltage*--Mode 4.

B. *LVRT Control under the Three-Phase Asymmetrical Voltage Sag*

An asymmetrical fault scenario is performed in the HIL platform to further demonstrate the operations of the HRES with the proposed LVRT control scheme. In order to better illustrate the experimental results of the three-phase signals, the data in the FPGA is recorded and transmitted to the host computer, as shown in Fig. 12.

As illustrated in Fig. 17, an asymmetrical fault happens, when the PCC voltage of phases *a*, *b* and *c* are decreased from 1 p.u. to 0.92 p.u. with 30° shift, 0.4 p.u. with 0° shift and 0.78 p.u. with -20° shift, respectively. During the fault period, the wind speed is 8.5 m/s, and the solar irradiance is 1000 W/m^2. The DC-Link voltage is increased from 1 p.u. to 1.07 p.u. to store extra renewable energy as the electrical potential energy of the capacitors. It is noted that the double-line-frequency power oscillation caused by the asymmetrical PCC voltage is absorbed by the DC-Link capacitor, as shown in the upper-left side of Fig. 17. In this scenario, control mode 2 is selected by the optimizer. Since the power curtailment of the PMSG can effectively guarantee the system safety, the MPPT operation of the PV array can stay intact, as shown in the bottom-left side of Fig. 17. By calculation, the positive-sequence component of the PCC voltage is decreased to 0.65 p.u. so that 0.7 p.u. reactive current is generated in the GSC output current of 1.1 p.u., as shown in the upper-right side of Fig. 17. As only positive-sequence component exists with the proposed control, the three-phase output current is symmetrical. When the fault is cleared, both the DC-Link voltage and the power generation of the PMSG are restored to their original values.

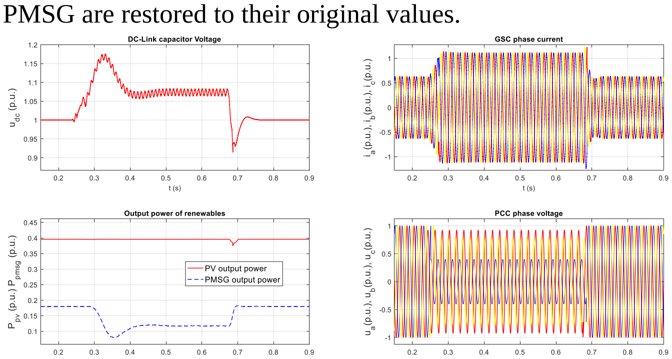

Fig. 17. HIL experiment waveforms of the HRES system under the asymmetrical voltage dip -- mode 2.

V. Simulation Studies on Comparisons Between the Proposed and Conventional LVRT Control

The HRES with the DC-shunt topology is built up in MATLAB-Simulink with specified system parameters shown in the Table III of the Appendix. In the simulation, the proposed and conventional LVRT control schemes are respectively applied on the faulted HRES with the same control parameters in the same controllers (see Table IV of the Appendix). For the conventional control scheme, the PMSG and the PV array are separately controlled without any coordination. However, the PMSG and the PV generator are coordinated for achieving the optimized operation with the proposed control.

A 0.56 p.u. voltage sag is simulated, when the wind speed and solar irradiance are 7*m/s* and *900W/m*^{2}, respectively. As shown in Fig. 18(b) and 18(d), the reactive currents and reactive powers generated in these two control schemes are the same (i.e. 0.8 p.u.). However, the proposed control outperforms the conventional controller at three aspects: (i) As illustrated in Fig. 18(c), the optimized solution to this fault with the proposed control is accelerating the rotor and simultaneously operating the PV array at the MPP. This can store more kinetic energy in the rotor mass. By contrast, the power generation of the PMSG and PV array are both curtailed by 48% with the conventional controller, which leads to a low efficiency and unnecessary energy waste. (ii) Direct output control is adopted in the proposed control. In this way, the active current output of the GSC with the proposed control scheme is of higher stability and faster dynamic response than that of the conventional control scheme, as illustrated in Fig. 18(b). (iii) With the proposed controller, certain electrical potential energy is stored in DC-link capacitor, as illustrated in Fig. 18(a). This regenerative energy can effectively accelerate the post-fault power recovery, as illustrated in Fig. 18(d).

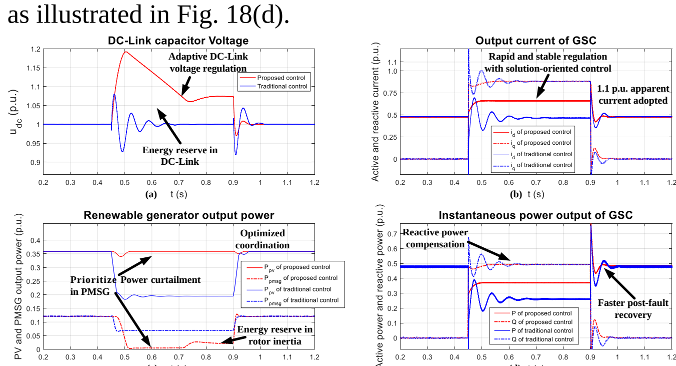

Fig. 18. Comparison waveforms with the proposed coordinative LVRT control and with the conventional LVRT control in the HRES.

VI. Conclusion

In this paper, a novel coordinative control scheme is proposed for the LVRT operation of the wind-PV HRES. This control scheme can fully exploit the energy buffering capability of the HRES for delivering the required power to the grid and optimizing the active power flows during faults. Specifically, it can coordinate the operations of four different controllers, namely, adaptive DC-Link voltage controller, PMSG KE controller, PV power curtailment controller, and blade pitch angle controller. With the embedded optimum operation strategy, the proposed control will improve the energy efficiency of the system and accelerate the post-fault recovery process. In addition, with the direct output control, the HRES can accurately provide the required active and reactive current with respect to various environmental conditions. Both the HIL experimental and simulation results have verified the functionality of the proposed control scheme.

VII. Appendix

TABLE I FOUR CONTROL MODES WITH THE ADJUSTABLE CONTROL STRUCTURE

Mode	PV	PMSG	DC-Link voltage	Voltage control output
1	MPP	ω^* $\beta = 0°$	>1 p.u.	I_{gdref} (MPPT control)
2	MPP	$> \omega^*$ $\beta = 0°$	>1 p.u.	ω_{ref} (direct output control)
3	De-loading	ω_{max} $\beta = 0°$	>1 p.u.	I_{pvref} (direct output control)
4	0	ω_{max} $\beta > 0°$	>1 p.u.	β_{ref} (direct output control)

TABLE II HARDWARE-IN-THE-LOOP VALIDATION PARAMETERS

Component	Specifications
Power rating	100kW PV & 160kW PMSG
Digital Controller	TMS320F28069 (80MHz)
RT sampling period	2 μs (8 ns in the FPGA)
Switching frequency	20 kHz (50 μs)
Main grid sampling period	500 μs
Grid frequency	50 Hz

TABLE III PARAMETERS OF SIMULATION WORKS

Component	Specifications
PV rated power	100kW at 1000W/m^2, 25^{o}C
PMSG rated power	160kW at 12m/s
PMSG max. rotating speed	9.6 rad/s (8 rad/s at 1 p.u.)
DC-Link capacitor	C_{dc} = 30 mF
Inverter output filter	L_f = 510 μH, R_f = 660 μΩ, LR filter
Rated phase voltage	220Vrms, 50Hz (Three-phase)
Nominal DC-Link voltage	750V
Switching frequency	20kHz
PCC rated current I_{rated}	560A (616A at 1.1 p.u.)

TABLE IV CONTROLLER PARAMETERS

Controller	Proportional Gain	Integral Gain
GSC current loop	0.2	30
DC-Link voltage loop for GSC current reference (Conventional)	2.3	50
TSC rotating speed loop	50	300
TSC current loop	0.05	5
DC-Link voltage loop for rotating speed reference (DOC)	0.02	0.1
ASC current loop	0.01	0.4
DC-Link voltage loop for PV current reference (DOC)	1.2	14
DC-Link voltage loop for pitch angle reference (DOC)	0.002	0.005
PMSG MPPT	Optimal tip speed ratio control	
PV array MPPT	Perturb & Observe method (1ms)	

Remarks: DOC is the abbreviation of direct output control.

References

[1] C. S. Lai, Y. Jia, L. L. Lai, Z. Xu, M. D. McCulloch, and K. P. Wong, "A comprehensive review on large-scale photovoltaic system with applications of electrical energy storage," *Renewable and Sustainable Energy Reviews*, vol. 78, pp. 439-451, 2017/10/01/ 2017.

[2] M. Wang, K. Mok, S. Tan, and S. Y. Hui, "Multifunctional DC Electric Springs for Improving Voltage Quality of DC Grids," *IEEE Transactions on Smart Grid*, vol. 9, no. 3, pp. 2248-2258, 2018.

[3] V. Khare, S. Nema, and P. Baredar, "Solar–wind hybrid renewable energy system: A review," *Renewable and Sustainable Energy Reviews*, vol. 58, pp. 2333, 2016/05/01/ 2016.

[4] F. Valenciaga and P. F. Puleston, "Supervisor control for a stand-alone hybrid generation system using wind and photovoltaic energy," *IEEE Transactions on Energy Conversion*, vol. 20, no. 2, pp. 398-405, 2005.

[5] V. Behravesh, R. Keypour, and A. A. Foroud, "Stochastic analysis of solar and wind hybrid rooftop generation systems and their impact on voltage behavior in low voltage distribution systems," *Solar Energy*, vol. 166, pp. 317-333, 2018/05/15/ 2018.

[6] M. F. M. Arani and Y. A. I. Mohamed, "Assessment and Enhancement of a Full-Scale PMSG-Based Wind Power Generator Performance Under Faults," *IEEE Transactions on Energy Conversion*, vol. 31, no. 2, pp. 728-739, 2016.

[7] Y. He, Z. Xu, and Y. Li, "A novel control scheme for enhancing low voltage ride through capability of solar generation," in *2017 China International Electrical and Energy Conference (CIEEC)*, 2017, pp. 129-134.

[8] F. Yang, L. Yang, and X. Ma, "An advanced control strategy of PV system for low-voltage ride-through capability enhancement," *Solar Energy*, vol. 109, pp. 24-35, 11// 2014.

[9] D. Xie, Z. Xu, L. Yang, J. Østergaard, Y. Xue, and K. P. Wong, "A Comprehensive LVRT Control Strategy for DFIG Wind Turbines With Enhanced Reactive Power Support," *IEEE Transactions on Power Systems*, vol. 28, no. 3, pp. 3302-3310, 2013.

[10] J. L. Sosa, M. Castilla, J. Miret, J. Matas, and Y. A. Al-Turki, "Control Strategy to Maximize the Power Capability of PV Three-Phase Inverters During Voltage Sags," *IEEE Transactions on Power Electronics*, vol. 31, no. 4, pp. 3314-3323, 2016.

[11] Y. Bae, T. K. Vu, and R. Y. Kim, "Implemental Control Strategy for Grid Stabilization of Grid-Connected PV System Based on German Grid Code in Symmetrical Low-to-Medium Voltage Network," *IEEE Transactions on Energy Conversion*, vol. 28, no. 3, pp. 619-631, 2013.

[12] V. Yaramasu, B. Wu, S. Alepuz, and S. Kouro, "Predictive control for low-voltage ride-through enhancement of three-level-boost and NPC-converter-

based PMSG wind turbine," *IEEE Trans. Ind. Electron.*, vol. 61, no. 12, pp. 6832–6843, Dec. 2014.

[13] C. T. Lee, C. W. Hsu, and P. T. Cheng, "A Low-Voltage Ride-Through Technique for Grid-Connected Converters of Distributed Energy Resources," *IEEE Transactions on Industry Applications*, vol. 47, no. 4, pp. 1821-1832, 2011.

[14] J. F. Conroy and R. Watson, "Low-voltage ride-through of a full converter wind turbine with permanent magnet generator," *IET Renew. Power Gen.*, vol. 1, no. 3, pp. 182–189, Sep. 2007.

[15] N. H. Saad, A. A. El-Sattar, and A. E.-A. M. Mansour, "Improved particle swarm optimization for photovoltaic system connected to the grid with low voltage ride through capability," *Renewable Energy*, vol. 85, pp. 181-194, 1// 2016.

[16] A. Q. Al-Shetwi, M. Z. Sujod, and F. Blaabjerg, "Low voltage ride-through capability control for single-stage inverter-based grid-connected photovoltaic power plant," *Solar Energy*, vol. 159, pp. 665-681, 2018/01/01/ 2018.

[17] N. Saadat, S. S. Choi, and D. M. Vilathgamuwa, "A Statistical Evaluation of the Capability of Distributed Renewable Generator-Energy-Storage System in Providing Load Low-Voltage Ride-Through," *IEEE Transactions on Power Delivery*, vol. 30, no. 3, pp. 1128-1136, 2015.

[18] P. Mohammadi, A. Eskandari, J. Milimonfared, and J. S. Moghani, "LVRT capability enhancement of single-phase grid connected PV array with coupled supercapacitor," in *2018 9th Annual Power Electronics, Drives Systems and Technologies Conference (PEDSTC)*, 2018, pp. 193-198.

[19] H. Tian, F. Gao, G. He, and G. Li, "Low voltage ride through of two-stage photovoltaic inverter with enhanced operational performance," in *2012 Twenty-Seventh Annual IEEE Applied Power Electronics Conference and Exposition (APEC)*, 2012, pp. 1995-2001.

[20] S. Alepuz, A. Calle, S. Busquets-Monge, S. Kouro, and B. Wu, "Use of stored energy in PMSG rotor inertia for low-voltage ride-through in back-to-back NPC converter-based wind power systems," *IEEE Trans. Ind. Electron.*, vol. 60, no. 5, pp. 1787–1796, May 2013.

[21] O. Noureldeen and A. M. A. Ibrahim, "Low-voltage ride-through capability enhancement of a grid-connected photovoltaic/wind hybrid power system," in *2017 Nineteenth International Middle East Power Systems Conference (MEPCON)*, 2017, pp. 786-795.

[22] V. Pagola-Torres, R. Peña-Gallardo, and J. Segundo-Ramírez, "Low voltage ride-through analysis in real time of a PV-Wind hybrid system," in *2015 IEEE International Autumn Meeting on Power, Electronics and Computing (ROPEC)*, 2015, pp. 1-6.

[23] L. Popavath and P. Kaliannan, "Photovoltaic-STATCOM with Low Voltage Ride through Strategy and Power Quality Enhancement in a Grid Integrated Wind-PV System," *Electronics*, vol. 7, no. 4, p. 51, 2018.

[24] A. Benali, M. Khiat, T. Allaoui, and M. Denaï, "Power Quality Improvement and Low Voltage Ride Through Capability in Hybrid Wind-PV Farms Grid-Connected Using Dynamic Voltage Restorer," *IEEE Access*, vol. 6, pp. 68634-68648, 2018.

[25] E.ON-Netz – Grid Code. *High and extra high voltage*, April 2006.

[26] M. D. A. Al-falahi, S. D. G. Jayasinghe, and H. Enshaei, "A review on recent size optimization methodologies for standalone solar and wind hybrid renewable energy system," *Energy Conversion and Management*, vol. 143, pp. 252-274, 2017/07/01/ 2017.

[27] G. Yang *et al.*, "Voltage rise mitigation for solar PV integration at LV grids," *Journal of Modern Power Systems and Clean Energy*, vol. 3, no. 3, pp. 411-421, 2015/09/01 2015.

[28] D. Zhou, Y. Song, Y. Liu, and F. Blaabjerg, "Mission Profile Based Reliability Evaluation of Capacitor Banks in Wind Power Converters," *IEEE Transactions on Power Electronics*, vol. 34, no. 5, pp. 4665-4677, 2019.

[29] X. Lyu, J. Zhao, Y. Jia, Z. Xu, and K. P. Wong, "Coordinated Control Strategies of PMSG-based Wind Turbine for Smoothing Power Fluctuations," *IEEE Transactions on Power Systems*, pp. 1-1, 2018.

[30] H. Geng, L. Liu, and R. Li, "Synchronization and Reactive Current Support of PMSG-Based Wind Farm During Severe Grid Fault," *IEEE Transactions on Sustainable Energy*, vol. 9, no. 4, pp. 1596-1604, 2018.

[31] K. Ma, W. Chen, M. Liserre, and F. Blaabjerg, "Power Controllability of a Three-Phase Converter With an Unbalanced AC Source," *IEEE Transactions on Power Electronics*, vol. 30, no. 3, pp. 1591-1604, 2015.

Yufei He (S'17) received the B.Eng. degree from Zhejiang University, China, in 2016. He is currently working toward the Ph.D. degree in the Department of Electrical Engineering, The Hong Kong Polytechnic University, Hong Kong. His research interests include power electronic control for grid-integration of renewables.

Ming-Hao Wang (S'15-M'18) received the B.Eng. (Hons.) degree in electrical and electronic engineering from the Huazhong University of Science and Technology, Wuhan, China, and the University of Birmingham, Birmingham, U.K. in 2012, and the M.Sc. and the Ph.D. degree, both in electrical and electronic engineering, from The University of Hong Kong, Hong Kong, in 2013 and 2017, respectively. He is currently a Postdoctoral Research Fellow with the Department of Electrical Engineering, Hong Kong Polytechnic University, Hong Kong. His research interests include dc power systems and power electronics.

Zhao Xu (M'06-SM'12) received B.Eng, M.Eng and Ph.D degree from Zhejiang University, National University of Singapore, and The University of Queensland in 1996, 2002 and 2006, respectively. From 2006 to 2009, he was an Assistant and later Associate Professor with the Centre for Electric Technology, Technical University of Denmark, Lyngby, Denmark. Since 2010, he has been with The Hong Kong Polytechnic University, where he is currently a Professor in the Department of Electrical Engineering and Leader of Smart Grid Research Area. He is also a foreign Associate Staff of Centre for Electric Technology, Technical University of Denmark. His research interests include demand side, grid integration of wind and solar power, electricity market planning and management, and AI applications. He is an Editor of the Electric Power Components and Systems, the IEEE PES Power Engineering Letter, and the IEEE Transactions on Smart Grid. He is currently the Chairman of IEEE PES/IES/PELS/IAS Joint Chapter in Hong Kong Section.